A 4D neonatal head model for diffuse optical imaging of pre-term to term infants

Sabrina Brigadoi [a],[*],[1], Paul Aljabar [b], Maria Kuklisova-Murgasova [b], Simon R. Arridge [c], Robert J. Cooper [d]

[a] Department of Developmental Psychology, University of Padova, Italy
[b] Centre for the Developing Brain and Department of Biomedical Engineering, Division of Imaging Sciences, King's College London, UK
[c] Department of Computer Science, University College London, UK
[d] Biomedical Optics Research Laboratory, Department of Medical Physics and Bioengineering, University College London, UK

ARTICLE INFO

ABSTRACT

Diffuse optical tomography is most accurate when an individual's MRI data can be used as a spatial prior for image reconstruction and for visualization of the resulting images of changes in oxy- and deoxy-hemoglobin concentration. As this necessitates an MRI scan to be performed for each study, which undermines many of the advantages of diffuse optical methods, the use of registered atlases to model the individual's anatomy is becoming commonplace. Infant studies require carefully age-matched atlases because of the rapid growth and maturation of the infant brain. In this paper, we present a 4D neonatal head model which, for each week from 29 to 44 weeks post-menstrual age, includes: 1) a multi-layered tissue mask which identifies extra-cerebral layers, cerebrospinal fluid, gray matter, white matter, cerebellum and brainstem, 2) a high-density tetrahedral head mesh, 3) surface meshes for the scalp, gray-matter and white matter layers and 4) cranial landmarks and 10-5 locations on the scalp surface. This package, freely available online at www.ucl.ac.uk/medphys/research/4dneonatalmodel can be applied by users of near-infrared spectroscopy and diffuse optical tomography to optimize probe locations, optimize image reconstruction, register data to cortical locations and ultimately improve the accuracy and interpretation of diffuse optical techniques in newborn populations.

© 2014 Elsevier Inc. All rights reserved.

Introduction

Diffuse optical tomography (DOT) is a functional imaging approach, which uses data from multiple sources and detectors of near-infrared light to reconstruct depth-resolved images of the concentration changes of oxy- (HbO) and deoxy- (HbR) hemoglobin (Culver et al., 2003; Dehghani et al., 2009; Gibson et al., 2005; Hielscher et al., 2002; White and Culver, 2010). These values can be calculated from changes in the light intensity measured between a source fiber and a detector fiber located several centimeters apart on the scalp (Boas et al., 2002; Jöbsis, 1977). A high number of channels, arranged densely on the scalp and with multiple source-detector distances in order to probe different depths inside the subject's head, allows the DOT technique to yield significant spatial information. In recent years DOT has been developing quickly, with the aim of improving the accuracy, the resolution and the sensitivity of the reconstructed images (Abdelnour et al., 2010; Boas et al., 2004; Gregg et al., 2010; Heiskala et al., 2012). Eggebrecht et al. (2012) and Zhan et al. (2012) have recently shown that, thanks to the recent advances in array design, signal analysis and head modeling, high-density DOT can achieve a spatial resolution comparable to that of functional magnetic resonance imaging (fMRI).

Diffuse optical techniques provide no information about the anatomical structure of the brain. However, accurate anatomical information is essential if the spatial information present in DOT data is to be fully exploited. Anatomical information not only allows meaningful visualization of the DOT images, but also helps the image reconstruction process itself by restraining the ill-posed inverse problem (Barnett et al, 2003; Boas and Dale, 2005; Guven et al., 2005; Pogue and Paulsen, 1998; Schweiger and Arridge, 1999; Zhang et al., 2005). Diffuse optical image reconstruction necessitates an accurate forward model, which maps a change in optical properties in the target object to a change in the DOT measurements. To produce an accurate forward model, a realistic, multi-layered head model of the different tissues of the human head, each assigned accurate optical properties, is essential. The position of the optical sources and detectors also has to be registered precisely to the head model in order for the forward problem to be solved (Perdue et al., 2012).

The best practice approach to performing DOT image reconstruction is therefore to register the DOT source and detector locations to each subject's individual MRI image, and use that MRI image to construct a subject-specific, multi-layered head model. However, acquiring an

* Corresponding author at: Biomedical Optics Research Laboratory, Department of Medical Physics and Bioengineering, Malet Place Engineering Building, University College London, Gower Street, London WC1E 6BT, U.K.
   E-mail address: s.brigadoi@ucl.ac.uk (S. Brigadoi).
[1] Present address: Biomedical Optics Research Laboratory, Department of Medical Physics and Bioengineering, University College London, U.K.

MRI image for every participant undermines the intrinsic advantages of the DOT technique, i.e. portability and applicability to challenging populations. The use of a generic head model, based on an MRI atlas, is a suitable and effective solution to this problem (Custo et al., 2010; Tsuzuki and Dan, 2013). A number of adult atlases have been applied to DOT (Custo et al., 2010; Ferradal et al., 2013; Habermehl et al., 2012; Tian and Liu, 2013). These include the Colin27 MRI atlas (Collins et al., 1998), which consists of a high-resolution MRI volume of a single individual and the non-linear ICBM152 atlas (Fonov et al., 2011), which constitutes a spatial average of 152 adults. When applied to DOT, each atlas must first be registered to each subject, usually by recording the location of a number of the subject's cranial landmarks and the DOT source and detector positions with a tracking system or with photogrammetric methods (Tsuzuki and Dan, 2013). As the corresponding cranial landmarks can be identified on the chosen atlas, the atlas volume can be transformed to match the subject's cranial dimensions (most simply by an affine transformation, see Singh et al. (2005) and Tsuzuki et al. (2012)). This registered atlas volume will then match the size, and to some extent the shape, of the individual's head, and an accurate forward model can be computed within this space. Using this process, an optical head model can enable an MRI-free approach to diffuse optical image reconstruction.

Both Cooper et al. (2012) and Ferradal et al. (2013) have shown that by employing a generic atlas head model, the localization error associated with DOT reconstruction in adults increases significantly when compared to that obtained using the subject's own MRI. However, atlas-based DOT can obtain a localization accuracy of ~10 mm, which is sufficient to identify the location of an activation within the gross cortical anatomy and even within a given cortical gyrus.

Diffuse optical techniques are widely used on term and preterm infants and have a long history of application to this population (Austin et al., 2006; Cooper et al., 2011; Elwell et al., 2005; White et al., 2012). This is partly due to the non-invasive nature of the technique and the fact that it is silent and applicable at the bedside (Fournier et al., 2012; Liao et al., 2012; Lloyd-Fox et al., 2010). DOT instrumentation can be applied in the Neonatal Intensive Care Unit (NICU), and recording can be continuous and long-term (Ancora et al., 2013; Lin et al., 2013). Infants are also very suitable for DOT techniques because of their smaller head sizes, thinner skulls and minimal hair, all of which make obtaining measurements of the brain more straightforward than is usually the case in adults.

Despite the widespread use of DOT in the neonatal field, there are a limited number of studies that have attempted to produce accurate infant head models (Dehaes et al., 2011; Fournier et al., 2012; Heiskala et al., 2009; White et al., 2012). Acquiring an MRI image of a newborn baby is challenging and is rarely performed unless clinically necessary. There are also difficulties in dealing with newborn MRIs because of a lack of established automatic tools to segment the neonatal MRI images into different tissue types (cerebrospinal fluid (CSF), gray (GM) and white matter (WM) for example). Indeed, automatic segmentation of the neonatal brain tissues remains a challenging problem because the contrast between the tissues is different and usually lower than that in adults and the within-tissue intensity variability is high (Altaye et al., 2008; Prastawa et al., 2005). The tools available for adult MRI segmentation cannot always be utilized without introducing significant errors (Wilke et al., 2003). As a result, there are a limited number of high-resolution MRI data-sets available for newborns and even fewer for pre-term babies.

Because the brain of the newborn infant is developing extremely quickly, accurate DOT reconstruction requires head models that are carefully age-matched. The brain structure of a 30 weeks PMA (post menstrual age) newborn is markedly different from that of a full term (40 weeks) baby (Battin and Rutherford, 2002). A single generic atlas, which can be applied to adults spanning a wide range of ages, will not be suitable for neonatal DOT. An atlas with age-specific infant MRIs, from pre-term to term, is therefore needed to produce suitable optical

head models. DOT image reconstruction can then be performed using the correct, age-matched anatomy.

A small number of term-age MRI atlases have been constructed and described in the literature. The atlas proposed by Shi et al. (2011) was built by registering and spatially averaging MRIs obtained from 95 infants aged between 38.7 and 46.4 weeks PMA to produce a single, term-age atlas volume. Similarly, the atlas proposed by Oishi et al. (2011) used data from 25 infants aged between 38 and 41 weeks PMA and the atlas proposed by Heiskala et al. (2009) used 7 infants aged between 39 and 41 weeks PMA. The atlas proposed by Sanchez et al. (2011) averaged MRIs acquired on 23 babies aged between 8 days to 29 days after birth.

Although these single-age atlases have many applications, the ideal neonatal atlas should be built from MRI data obtained over a wide pre-term to term age range, and would ideally include enough data at each age to allow an atlas to be dynamically produced for any arbitrary age within that range. The atlas proposed by Kuklisova-Murgasova et al. (2011) does just that. Using MRI images recorded on 142 infants ranging from 29 weeks PMA to 47 weeks PMA and using a weighted averaging approach this atlas allows the production of tissue probability maps for any age in this range, and the resulting volumes are publicly available for 29 to 44 weeks in one week intervals (www.brain-development.org).

Although this 4D atlas provides a great resource for producing age-matched head models for DOT, there is one significant difficulty preventing the use of the volumes that are currently available online. Because DOT requires a forward model to be computed based on the scalp locations of each source and detector, a model of the extra-cerebral tissues is essential. For a number of reasons, including data protection and a more accurate registration and segmentation, the scalp and skull layers visible in the MRI data are usually stripped out of the image prior to that data being included in the atlas. In order to produce DOT head models, it is first necessary to retrieve the extra-cerebral tissue layers.

The aim of this paper is to present a 4D optical head model for pre-term and term newborns ranging from 29 weeks PMA to 44 weeks PMA that can be used by researchers to perform DOT image reconstruction on an accurate, age-matched anatomy. Each step of the construction of the 4D optical head model is presented and discussed. The final package, available online at www.ucl.ac.uk/medphys/research/4dneonatalmodel contains, for each age: 1) a multi-layered tissue mask which identifies extra-cerebral layers, cerebrospinal fluid, gray matter, white matter, cerebellum and brainstem, 2) a high-density volumetric, multi-layered tetrahedral head mesh, 3) The scalp, white matter and gray matter surface meshes and 4) all the coordinates for the 10-5 positions and cranial landmarks on the scalp.

Materials and methods

Subjects

The MRI atlas on which we based our models was built using 324 (160 female) T2-weighted fast-spin echo images acquired on 3T Philips Intera system with MR sequence parameter TR = 1712 ms, TE = 160 ms, flip angle 90° and voxel size $0.86 \times 0.86 \times 1$ mm. The original atlas (Kuklisova-Murgasova et al., 2011) was built using 142 T2-weighted images; new images have been acquired since its release and have been added to the average volumes on which our head models are based. The age range of the newborns at the time of scanning was 26.7 to 47.1 weeks PMA.

MRI atlas pre-processing

Because of the necessity of including scalp and skull information in the final atlas, the same process of affine registration to an average reference space and voxel-wised weighted intensity averaging, with

weights obtained with a Gaussian kernel regression, described in Kuklisova-Murgasova et al. (2011), was performed on all 324 T2-weighted images, without removing the extra-cerebral layers. An averaged T2-weighted image including the extra cerebral tissues was therefore obtained for each week from 29 to 44 weeks PMA yielding a total of 16 volumes, a subset of which is shown in Fig. 1.

As part of the pre-processing of the MRI volumes, a structural segmentation of the different brain tissues into 87 regions was performed. This segmentation was carried out using the approach of Ledig et al. (2012). The method employs a set of MRI atlases and corresponding manual segmentations for all 87 structures. For each target image, all atlas MRI images are registered to the target using a non-rigid registration. This results in a set of deformations that can be used to map the atlas structures onto the target's native space. For each structure, a voxel-wise spatial prior probability map is estimated by averaging the corresponding masks of that structure for all the mapped atlases. The spatial priors are then used in conjunction with the target images' intensity information to optimize the segmentation of all 87 structures.

Each brain-extracted individual MR scan was thus segmented in its native space. The resulting segmented images underwent an affine transformation to the average T2 age-matched image. The final structural segmentation mask for each age was then obtained by assigning each voxel to the region that it is most commonly defined as in the individual segmentations.

Multi-layer tissue mask

To produce a head model of fundamental tissue types, for which the optical properties of absorption coefficient and scattering coefficient are available, the 87 identified brain regions were divided into 5 tissues: cerebrospinal fluid (CSF), gray matter (GM), white matter (WM), as well as cerebellum and brainstem.

The segmentation of the extra-cerebral tissues was performed with FSL (http://fsl.fmrib.ox.ac.uk/fsl/fslwiki/) on the average T2 image for each age. The BET (Brain Extraction Tool) routine was used, including the function BET2, which isolates the brain, and the function BETSURF, which separates the outer scalp and inner skull surfaces (Jenkinson et al., 2005). Since the scalp and skull in neonates are very thin and are difficult to distinguish in T2 images, the scalp and skull tissues

were merged into a single extra-cerebral tissue (ECT) layer. These segmentation processes identified the brain and the inner skull surface. The extra-cerebral CSF layer was defined by the gap between the outer gray matter and the inner skull surfaces. Voxels between these two structures were labeled as CSF.

The final multi-layer tissue masks (consisting of ECT, CSF, GM, WM, cerebellum and brainstem tissues) are displayed in Fig. 2 for a sub-set of ages. All multi-layered tissue masks were inspected by a clinical neonatologist in order to prevent major segmentation errors and insure that the development of the brain is accurate.

Volumetric tetrahedral mesh construction

A high-density, volumetric, tetrahedral multi-layered mesh was created for each of the 16 ages using the multi-layered tissue mask described above. This was performed using the iso2mesh toolbox (Fang and Boas, 2009a), with the CGAL mesher option (http://www.cgal.org), which involves using the Computational Geometry Algorithms Library for direct mesh generation. This is a C++ library that allows fast creation of a complex mesh from a multi-region volume. The maximum element volume size was set to 1 mm^3 and the maximum radius of the Delaunay sphere was set to 1 mm. The tetrahedral meshes for a subset of ages are shown in Fig. 3.

In order to assess the quality of the created volumetric meshes, the Joe–Liu quality index was computed for every tetrahedron for all ages (Liu and Joe, 1994):

$$q_{vol} = \frac{12 * (3 * vol)^{\frac{2}{3}}}{\Sigma_{0 \leq i \leq j \leq 3} l_{i,j}^2}$$

where vol is the tetrahedral volume and $l_{i,j}$ are the lengths of the edges of the tetrahedron. This metric is equal to 1 for equilateral tetrahedra and tends to 0 for degenerated tetrahedra. A high quality mesh is expected to score high q_{vol} values.

GM, WM and scalp surface mesh construction

A surface mesh for each of the GM, WM and scalp layers was created for each age of the atlas using the iso2mesh toolbox. High density GM
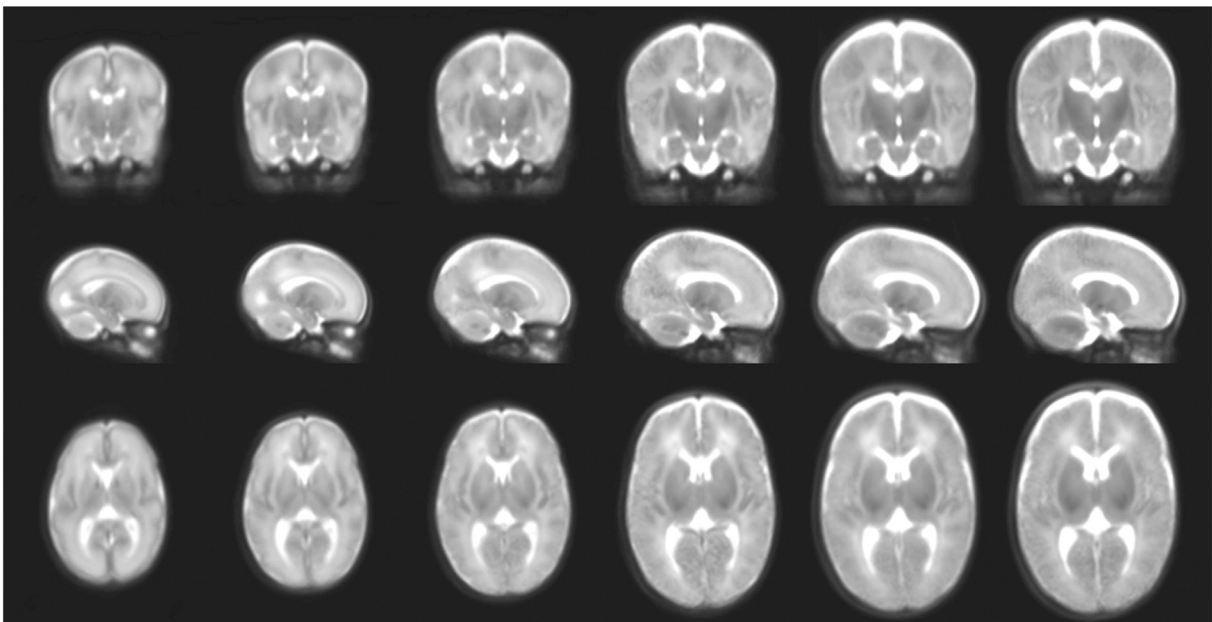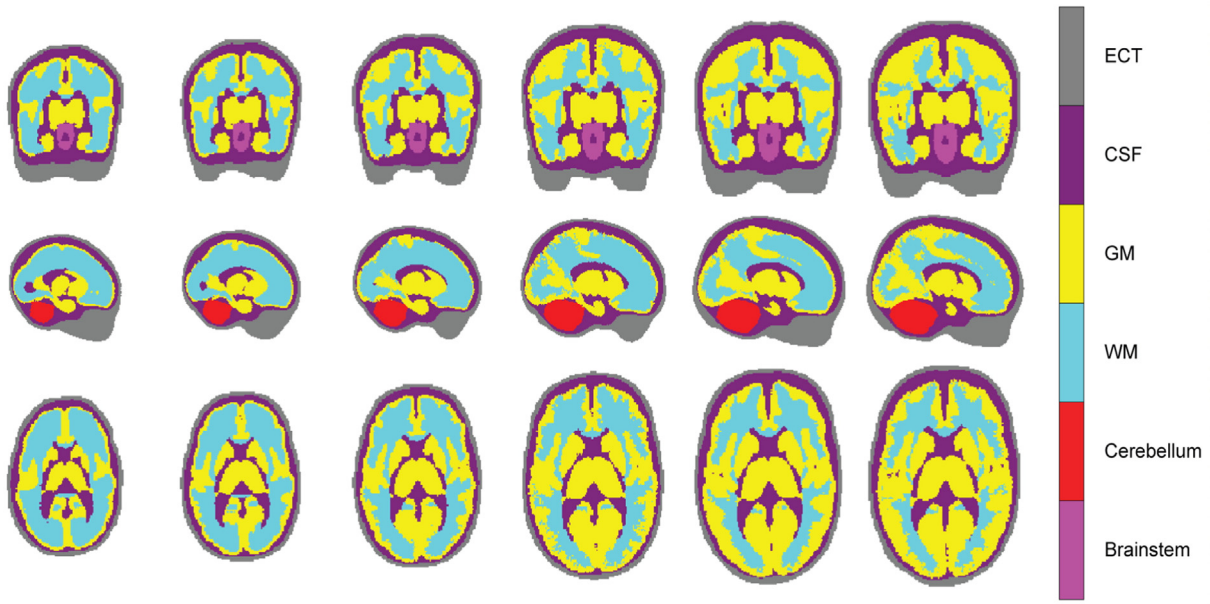

Fig. 1. T2-weighted average MRIs for example ages (29, 32, 35, 38, 41 and 44 weeks PMA). In the first row a coronal view of the MRI volume is shown, the second row shows a sagittal view and the third row shows an axial view.
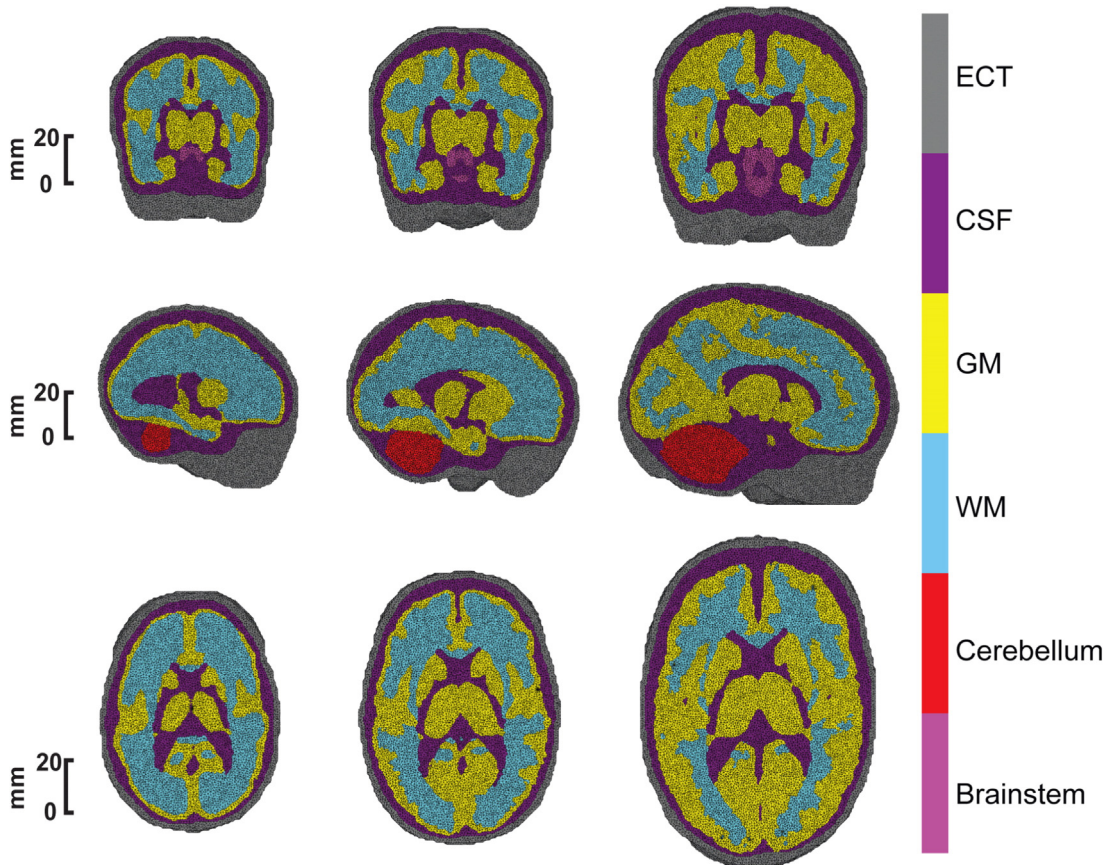
Fig. 2. Multi-layered tissue masks for example ages (29, 32, 35, 38, 41 and 44 weeks PMA). The first row shows a coronal view of the mask, the second row shows a sagittal view and the third an axial view. In gray is displayed the extra-cerebral tissue (ECT), in purple the CSF, in yellow the GM, in cyan the WM, in violet the brainstem and in red the cerebellum.

and scalp surface meshes were created from the tissue masks using the CGAL meshing procedure. In order to preserve the finer details of the WM layer, particularly the corpus callosum, it was necessary to first produce a high-density volumetric mesh of the WM tissue. The WM surface mesh was then extracted by selecting only the external nodes of the volumetric mesh.

In order to obtain surface meshes with a density low enough to make their use computationally straightforward, but high enough to maintain

Fig. 3. Multi-layered volumetric tetrahedral meshes for example ages (29, 35, and 44 weeks PMA). The first row shows a coronal view of the mesh, the second row shows a sagittal view and the third show an axial view. In gray is displayed the extra-cerebral tissue (ECT), in purple the CSF, in yellow the GM, in cyan the WM, in violet the brainstem and in red the cerebellum.

the anatomical details of the tissues, a down-sampling procedure was performed; only 30% of the initial nodes were kept. A low-pass filter, which Bade et al. (2006) have shown to be the best volume preserving smoothing algorithm, was also applied to smooth the surface. This process better preserves anatomical details than the direct production of a lower-density surface mesh. The mean face area of each mesh before and after the down-sampling and smoothing procedure was computed, as was the mean Hausdorff distance across ages between the high-density mesh and the down-sampled and smoothed mesh. The results confirmed that the macrostructure of each mesh was preserved by the down-sampling and smoothing procedure. The mean increase in face area was <1 mm², and the mean Hausdorff distance across ages between the meshes was less than 2 mm for the scalp and GM meshes and less than 2.6 mm for the WM mesh. An example of the surface mesh for all three layers is shown in Fig. 4 for selected ages.

The quality of the surface meshes was assessed by computing for every triangle of each mesh the following quality index (Field, 2000):

$$q_{surf} = \frac{4 * \sqrt{3} * A}{l_1^2 + l_2^2 + l_3^2}$$

where A is the area of the triangle and $l_{1,2,3}$ are the lengths of its sides. As for the volumetric mesh case, this quality metric equals 1 when the triangle is equilateral, and tends to 0 for a degenerated triangle. A high quality mesh should give high q_{surf} values.
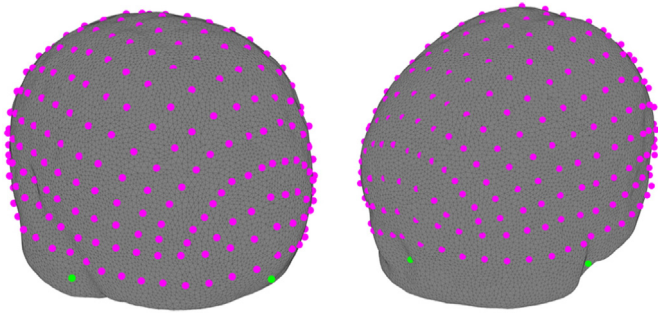
Cranial landmarks and 10-5 positions

For every age, the coordinates of cranial landmarks corresponding to the inion (Iz), nasion (Nz) and left and right pre-auricular points (ALAl and ARAr) were manually determined using FreeSurfer (http://surfer.nmr.mgh.harvard.edu/) to visualize the surface. The 3D rendering tool creates a 3D rendering of the scalp surface starting from the average T2 MRI volume, which allows the ears and the nose of the average MRI volume to be identified. The landmark coordinates derived from the T2 image are then transferred to the volumetric head mesh; the coordinates of the nearest node of the mesh are assigned as the final landmarks' coordinates.

The 10-5 system is an EEG-based convention for electrode positioning (Oostenveld and Praamstra, 2001). It is a high-density system, which comprises 345 scalp locations. Since many researchers in the DOT community use the 10-5 system or lower density versions (10-10 or 10-20) to position their optodes (Jurcak et al., 2007), we calculated, for every age, the coordinates of the corresponding 10-5 locations. Given three points on the mesh surface (for example Al, Ar and the vertex, Cz), a plane can be created and the intersection between the plane and the outer surface of the volumetric mesh (plus or minus some threshold width α) defines a curve along the scalp surface (in this example, the curve from Al to Ar via Cz). Each curve was smoothed using a 3D spline interpolation using only 1 in 4 of the surface nodes, which intersect the plane. The 10-5 locations along that curve can then be calculated by dividing the total length of the curve into 5% intervals.
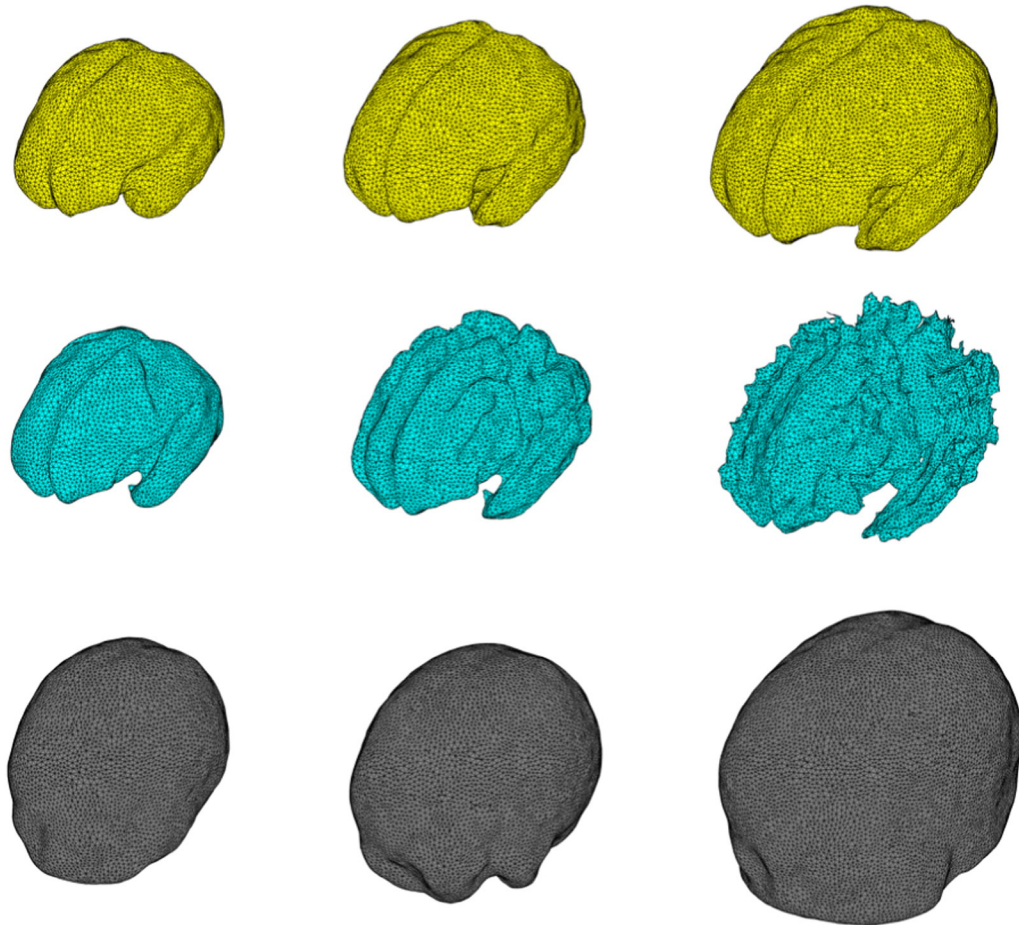
Fig. 4. Surface meshes for GM, WM, and scalp for example ages (29, 35 and 44 weeks PMA). In the first row the GM surface mesh is displayed for each age. In the second row, the WM surface mesh is displayed for the three selected ages. In the third row, the scalp surface mesh is shown for the three ages. Note the increasing convolution of the WM surface, and to a lesser extent the GM surface, with age.

Fig. 5. Cranial landmarks (in green) and 10-5 positions (in magenta) superposed on the 44-weeks baby scalp mesh. In the left figure, Al, and inion can be observed, while nasion is visible in the right figure.

An example of the 10-5 locations and the cranial landmarks positioning on a head model for a single age are shown in Fig. 5.

Demonstration of the head models in use

As a demonstration of the application of our head models to diffuse optical imaging, we employed three different methods of modeling photon transport and solving the forward problem. In our tetrahedral meshes, we applied both a Monte Carlo approach (using the MMC package (http://mcx.sourceforge.net)) and the Finite Element Method (using TOAST (http://web4.cs.ucl.ac.uk/research/vis/toast)). We also applied a voxel-based Monte Carlo method (using the MCX package (http://mcx.sourceforge.net)) to model photon transport and solve the forward problem in the multi-layer tissue mask rather than in tetrahedral mesh. A simulated set of sources and detectors were placed on the Al–Ar line (sources at C5, C1, C2 and C6 and detectors at T7, C3, C4 and T8), to provide a total of 4 channels with same source-detector separation. Optical properties were assigned to every tissue layer as follows (absorption coefficient (mm^{-1}), reduced scattering coefficient (mm^{-1}) and refractive index, respectively): 0.017, 1.75, 1.3 for the ECT layer, 0.0041, 0.032, 1.3 for the CSF layer, 0.048, 0.5, 1.3 for the GM layer, and 0.037, 1, 1.3 for the WM, cerebellum and brainstem layers (Dehaes et al., 2011).

Results

In Table 1 a summary of the properties and quality indices of the computed volumetric meshes is reported for each age. The total number of nodes, faces and elements is also reported. As expected, the number of nodes, faces and elements increases with age. In the 5th column of the table the mean Voronoi volume (across all nodes) with its standard deviation is shown. For all ages, the volume is lower than 1 mm³,

confirming the high density of the mesh. In the last column the mean Joe–Liu quality index q_{vol} (computed across all tetrahedrons) is reported with its standard deviation. All meshes achieve a high quality score. The lowest q_{vol} index observed in any of the meshes is 0.1. The vast majority of elements are close to equilateral (88.4% of the q_{vol} indices are higher than 0.7) and no elements are completely degenerated.

A summary of the properties of the GM, WM and scalp surface meshes is reported in Table 2. The number of nodes and faces, as well as the mean area of the triangles with its standard deviation, is shown for every age. As in the volumetric case, the number of nodes and faces generally increases with age.

The results achieved by the GM, WM and scalp surface meshes for the quality index q_{surf} are reported in Table 3. All the surface meshes are of a very high quality. The lowest q_{surf} index observed in any of the surface meshes is 0.02. The vast majority of faces are equilateral (97.9% of the q_{surf} indices are higher than 0.7) and no faces are completely degenerated.

In Fig. 6 the results achieved with both MMC (a), TOAST (b) and MCX (c) are displayed for a representative age, in the form of the sensitivity distribution of the 4 channels of our simulated optode array. The three forward models are comparable, with a high sensitivity observed near the location of each optode and a decreasing sensitivity with depth. Note the characteristic shape of the photon measurement density function. Such forward solutions can be inverted and used to reconstruct images of optical data acquired with the corresponding optode configuration.

Discussion

Thanks to steady advances in perinatal medicine, the survival rate for preterm infants has considerably increased in the last 3 decades. According to the report of the European Foundation for the Care of Newborn Infants (EFCNI) most European countries have preterm birth rates of 7% or above. Although the mortality of preterm babies is decreasing, long-term complications due to prematurity are still a significant challenge (Costeloe et al., 2012). The increasing accuracy and applicability of functional imaging technologies, including diffuse optical tomography are likely to play an increasingly significant role in the monitoring of pre-term development.

The creation of the 4D optical head model described here is an important step in the development of DOT in neonatal imaging. It allows researchers to choose, for every newborn measured with DOT, an accurate, age-matched head model and perform the image reconstruction process using an anatomy that is as close as currently possible to that of the studied infant. This constitutes the current best-practice approach to diffuse optical image reconstruction for the neonatal population when individual MRI data is not available.

Table 1
For every age, the properties of the volumetric mesh (number of nodes, faces, elements and the Voronoi volume) are reported. In the last column, the Joe–Liu quality index is also shown.

Age (week)	N nodes	N faces	N elements	Mean Voronoi volume ± std (mm³)	Mean q_{vol} ± std
29	382,625	491,958	2,284,103	0.836 ± 0.256	0.830 ± 0.104
30	385,532	495,868	2,300,908	0.837 ± 0.255	0.831 ± 0.103
31	401,735	531,426	2,400,077	0.835 ± 0.253	0.830 ± 0.104
32	423,051	560,160	2,528,645	0.835 ± 0.254	0.830 ± 0.104
33	442,782	591,316	2,647,723	0.836 ± 0.253	0.830 ± 0.104
34	481,464	634,968	2,882,826	0.836 ± 0.253	0.830 ± 0.104
35	512,514	689,286	3,072,358	0.835 ± 0.254	0.828 ± 0.105
36	566,593	761,656	3,401,223	0.836 ± 0.254	0.828 ± 0.105
37	636,061	862,276	3,824,980	0.833 ± 0.256	0.827 ± 0.107
38	716,509	962,526	4,314,759	0.831 ± 0.259	0.826 ± 0.107
39	784,391	949,436	4,726,239	0.839 ± 0.255	0.829 ± 0.106
40	805,537	933,424	4,852,397	0.844 ± 0.251	0.830 ± 0.104
41	833,782	951,462	5,025,079	0.844 ± 0.253	0.830 ± 0.105
42	866,808	970,150	5,227,709	0.846 ± 0.251	0.831 ± 0.104
43	889,455	1,006,512	5,366,655	0.843 ± 0.255	0.829 ± 0.106
44	906,023	1,055,900	5,469,235	0.840 ± 0.256	0.828 ± 0.107

Table 2
Number of nodes and faces, as well as mean area of the triangles and its standard deviation, for all ages for the GM, WM and scalp surface meshes.

Age (week)	GM surface mesh			WM surface mesh			Scalp surface mesh		
	N nodes	N faces	Mean area $\pm$ std (mm^2)	N nodes	N faces	Mean area $\pm$ std (mm^2)	N nodes	N faces	Mean area $\pm$ std (mm^2)
29	6037	12,078	1.335 $\pm$ 0.406	8794	17,584	1.283 $\pm$ 0.385	7916	15,828	1.456 $\pm$ 0.424
30	5820	11,640	1.404 $\pm$ 0.424	8950	17,906	1.293 $\pm$ 0.378	8199	16,394	1.411 $\pm$ 0.411
31	6413	12,830	1.370 $\pm$ 0.422	9951	19,904	1.272 $\pm$ 0.387	8217	16,430	1.447 $\pm$ 0.420
32	6773	13,570	1.378 $\pm$ 0.422	10,723	21,442	1.256 $\pm$ 0.382	8613	17,222	1.434 $\pm$ 0.410
33	7471	14,946	1.347 $\pm$ 0.409	11,520	23,056	1.231 $\pm$ 0.389	8980	17,956	1.430 $\pm$ 0.413
34	8017	16,050	1.329 $\pm$ 0.419	12,636	25,294	1.211 $\pm$ 0.386	9549	19,094	1.420 $\pm$ 0.413
35	8577	17,162	1.376 $\pm$ 0.414	13,949	27,910	1.181 $\pm$ 0.393	9927	19,850	1.431 $\pm$ 0.413
36	10,457	20,926	1.248 $\pm$ 0.382	16,002	31,997	1.150 $\pm$ 0.396	10,469	20,934	1.450 $\pm$ 0.424
37	10,831	21,678	1.310 $\pm$ 0.404	18,350	36,711	1.113 $\pm$ 0.406	11,344	22,684	1.447 $\pm$ 0.418
38	11,285	22,574	1.355 $\pm$ 0.430	21,040	42,205	1.073 $\pm$ 0.411	12,274	24,544	1.453 $\pm$ 0.413
39	11,480	22,956	1.393 $\pm$ 0.424	19,678	39,424	1.125 $\pm$ 0.405	13,090	26,176	1.452 $\pm$ 0.417
40	11,813	23,626	1.389 $\pm$ 0.421	18,983	37,992	1.163 $\pm$ 0.404	13,453	26,902	1.448 $\pm$ 0.417
41	11,885	23,766	1.396 $\pm$ 0.419	18,794	37,630	1.163 $\pm$ 0.405	13,721	27,438	1.447 $\pm$ 0.416
42	12,195	24,394	1.390 $\pm$ 0.420	19,189	38,448	1.149 $\pm$ 0.406	13,933	27,862	1.459 $\pm$ 0.423
43	12,444	24,888	1.383 $\pm$ 0.422	19,825	39,745	1.114 $\pm$ 0.413	13,938	27,872	1.480 $\pm$ 0.432
44	12,916	25,836	1.356 $\pm$ 0.421	21,440	43,001	1.073 $\pm$ 0.424	14,306	28,608	1.462 $\pm$ 0.424

Image reconstruction for diffuse optical techniques requires an accurate forward model, which, by modeling photon migration through the tissues from the array of sources predicts how the DOT data will change given a change in tissue optical properties. The more realistic the head model, the more accurate the forward model and the more accurate the resulting DOT images. Our 4D head model provides a realistic, high quality volumetric head mesh for every age from 29 weeks PMA to 44 weeks PMA, at one-week intervals (Fig. 3).

The process of applying this optical head model first requires knowledge of the locations of the cranial landmarks and the source and detector fibers on the scalp of the infant under examination. These positions can be measured using an electromagnetic tracking system or via photogrammetry. As an alternative to measuring each fiber position individually, which can be time consuming, it is possible to position the fibers relative to the subject's 10-5 locations. As these positions are provided directly for each age of our 4D head model, the position of each source and detector fiber on the mesh can be easily determined.

Once the cranial landmarks have been measured, the age-matched head model must be registered to the individual baby's head size and shape. The simplest approach to this registration is to define an affine transformation matrix between the baby's measured cranial landmarks and the equivalent locations provided for each age of the head model (Singh et al., 2005; Tsuzuki et al., 2012).

Table 3
For every age the mean value of q_{surf} and its standard deviation are displayed for GM, WM and scalp surface meshes.

Age (week)	GM surface mesh	WM surface mesh	Scalp surface mesh
	Mean q_{surf} $\pm$ std	Mean q_{surf} $\pm$ std	Mean q_{surf} $\pm$ std
29	0.928 $\pm$ 0.078	0.928 $\pm$ 0.076	0.931 $\pm$ 0.070
30	0.929 $\pm$ 0.073	0.931 $\pm$ 0.073	0.931 $\pm$ 0.071
31	0.927 $\pm$ 0.077	0.928 $\pm$ 0.073	0.931 $\pm$ 0.071
32	0.928 $\pm$ 0.075	0.929 $\pm$ 0.072	0.933 $\pm$ 0.069
33	0.928 $\pm$ 0.075	0.925 $\pm$ 0.078	0.932 $\pm$ 0.068
34	0.925 $\pm$ 0.080	0.926 $\pm$ 0.079	0.931 $\pm$ 0.070
35	0.928 $\pm$ 0.075	0.921 $\pm$ 0.083	0.933 $\pm$ 0.069
36	0.927 $\pm$ 0.074	0.919 $\pm$ 0.090	0.931 $\pm$ 0.070
37	0.927 $\pm$ 0.077	0.911 $\pm$ 0.099	0.932 $\pm$ 0.069
38	0.924 $\pm$ 0.080	0.905 $\pm$ 0.107	0.933 $\pm$ 0.069
39	0.927 $\pm$ 0.075	0.913 $\pm$ 0.096	0.932 $\pm$ 0.069
40	0.928 $\pm$ 0.074	0.918 $\pm$ 0.092	0.932 $\pm$ 0.070
41	0.928 $\pm$ 0.075	0.917 $\pm$ 0.093	0.934 $\pm$ 0.068
42	0.928 $\pm$ 0.076	0.916 $\pm$ 0.093	0.932 $\pm$ 0.070
43	0.927 $\pm$ 0.076	0.909 $\pm$ 0.103	0.932 $\pm$ 0.070
44	0.926 $\pm$ 0.078	0.902 $\pm$ 0.113	0.932 $\pm$ 0.070

Once the age-matched head mesh has been registered to the subject, and the source and detector locations on the mesh have been determined, relevant optical properties can be assigned to the tissues composing the volumetric head mesh, to take into account the different absorption and scattering coefficients of the different tissue types. It is known that adult and neonatal tissues have different optical properties (Fukui et al., 2003). Selecting accurate optical properties is important, but the availability of neonatal optical properties is still very limited. A sensitivity analysis to quantify the errors introduced by the use of incorrect optical properties using the head models presented here would be beneficial, as would thorough measurement of the optical properties of neonatal tissues across the NIR spectrum.

It should be noted that the optical properties of the scalp and skull in neonates are thought to be very similar. Dehaes et al. (2011), employ values of $\mu_a = 0.018$ mm^{-1} for the scalp and 0.016 mm^{-1} for the skull, $\mu_s' = 1.9$ mm^{-1} for the scalp and 1.6 mm^{-1} for the skull. As a result, our determination of a single ECT layer (as opposed to independent scalp and skull layers) is unlikely to have a significant impact on photon transport. To strengthen this assumption, we have begun a series of Monte Carlo simulations in simplified, multi-layered slab models. By comparing the sensitivity distribution produced in a model containing a single ECT layer to those obtained in models with varying thicknesses of scalp and skull layers, the impact of employing a single ECT layer can be quantified. While more analysis is required, preliminary results suggest that the percentage difference between the sensitivity distribution of the ECT-only model and the scalp/skull models in the GM and WM layers was below 10% for the majority of voxels and below 20% for all voxels. These error values imply that imposing a division of scalp and skull in our 4D head model will have a nominal impact on the resulting diffuse optical images. We recommend that users of our 4D neonatal head model approximate the optical properties of the ECT layer using an average of the available values for scalp and skull tissues, as performed above.

Once the tissue optical properties are defined, a Monte Carlo simulation (performed using, for example, the MMC package (Fang, 2010; Fang and Kaeli, 2012)) or the finite element method (performed using, for example, the TOAST package (Schweiger and Arridge, 2014)), can be used to model photon migration in the volumetric head model mesh and to produce a forward model (Arridge, 2011; Gibson et al., 2005) (Fig. 6).

Alternatively, the forward model can be solved, in a computationally efficient and accurate way using the Boundary Element Method (BEM) (Elisee et al., 2011). BEM solves the differential equations of the forward problem using Green's theorem to transform them into a set of integral equations defined only on the surfaces of layers within a volume. Using this approach, the matrix dimensionality of the forward problem is
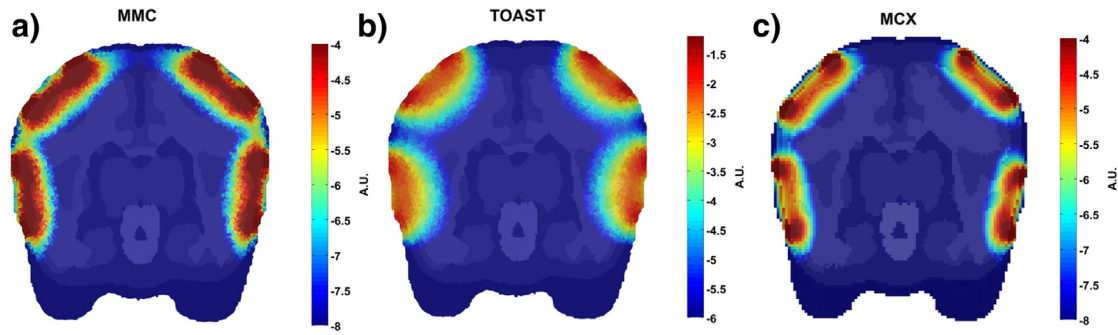
Fig. 6. MMC (a), TOAST (b) and MCX (c) simulation results. A mesh cut at the AlAr plane of the 35 week baby is shown. The log of the sensitivity is displayed for the 4 channels in each case. High sensitivity indicates that a high number of photons pass through that element on their way to a detector. Note how the sensitivity decreases with increasing depth.

considerably reduced. This method assumes that the volume between two surfaces is a piece-wise constant domain and therefore BEM does not require a volumetric mesh but only surface meshes. This is one further reason why the package described here includes scalp, GM and WM surface meshes.

Another alternative for the forward model solution is to use a voxel-based Monte Carlo approach (performed using the MCX package for example (Fang and Boas, 2009b)) (Fig. 6). This is one reason why the package described here includes the multi-layer tissue mask, which can easily be used to run the voxel-based Monte Carlo simulation. The package proposed here, therefore, allows the user to choose their preferred method of solving the forward problem. As shown in Fig. 6, the forward solutions produced by FEM and Monte Carlo approaches will be different, simply because these algorithms are based on fundamentally different models. The difference between the results obtained using MMC and MCX, is likely due to an inaccurate geometric representation of the head tissues in the voxel space, which may negatively impact the accuracy of the solution (Fang, 2010). The strength of mesh-based approaches is the ability to model continuously varying complex media.

The neonatal brain develops extremely quickly. In Fig. 1 it is evident how the brain and head of the newborn is not only increasing in size going from 29 weeks PMA to 44 weeks PMA, but also the shape and contrast between different tissues are changing rapidly. It is clear in Fig. 1 that the T2 image of a term baby (39–41 weeks PMA) exhibits higher contrast between GM and WM compared to the T2 image of a preterm newborn (29 weeks PMA), where the high water content produces long T1 and T2 times and thus a low signal in the WM part of the image.

The development of the brain is even more evident in the GM and WM surface meshes shown in Fig. 3. The cortical surface of a 29 week PMA infant is relatively smooth (Battin and Rutherford, 2002) but cortical folds rapidly develop between 39 and 40 weeks PMA. The cortical folding apparent in our GM surface meshes is noticeably less than that of individual infant MRIs of ~35–44 weeks PMA. This detail is likely to have been lost in the averaging process used to obtain the atlas because of the large variability between different infants. However, the GM surface meshes do show the cortical folding increasing with age. The GM surface mesh for the 29 week baby is very smooth, while the GM surface mesh for a term baby (39–41 weeks PMA) clearly shows some of the main sulci in the parietal cortex and evidence of the central gyrus.

Although our average cortical meshes do not exhibit the sulci and gyri as clearly as an individual MRI of that age, the smoothing of these features due to the spatial averaging of T2 images is representative of the anatomical variation across infants at that age. While it would be possible to base each mesh on an individual (non-averaged) MRI that would maintain denser cortical folding, to reconstruct DOT images using such a mesh and present those images on those cortical folds would bias those images, and would ultimately be misleading.

The WM surface mesh displays a clear development from preterm to term neonates. The WM appears as a smooth surface in the extreme

preterm baby, and this smoothness is likely due to both the underdevelopment of the WM and of the cortical GM, where folding has yet to take place. In the term baby, the GM folding has already started and consequently the boundary between the WM and GM becomes more complex, exhibiting higher curvature.

The FSL approach that we employed to isolate the extra-cerebral tissues has been validated in adults but has also been used previously with infants (Sanchez et al., 2011). Tissue contrasts in infant T2 MRI images are markedly different from those of the adult, and T2 images do not produce high contrast for extra-cerebral tissues. The BETSURF tool works preferentially with T1 images, and its performance is improved by using both T1s and T2s. In our case, only T2 images were available; T2 contrast images are the most commonly applied to neonates in clinical circumstances. As a result, it was not possible to separate the scalp and skull layers and the BETSURF procedure may overestimate or (more likely) underestimate the thickness of the extra-cerebral layer. While the ECT layer could be explicitly separated into two by modeling the skull–scalp boundary, such an approach would require additional assumptions that are not justified by the available MRI data and would be impossible to validate. If both T1 and T2 images were available, the segmentation of the extra-cerebral tissues would likely be more accurate and it may even be possible to separate the scalp and skull layers. In the future it may be possible to improve the identification of extra-cerebral tissues by designing an MRI sequence that is specifically tuned to the problem of seeking accurate optical head models.

The T2 images from individual infants were brain co-aligned in order to obtain an average T2 image for each age. As a result, there is greater spatial variability in structures which are distant from the brain. This particularly affects the lower regions of the head, which exhibit poor contrast in the average T2 images. As a result, the shape of the external surface of the extra-cerebral tissue layer on the under-side of the head is not reliable. However, this inaccuracy will have no impact on optical brain imaging applications.

Dehaes et al. (2011) have shown that including the temporal fontanel in the model of the newborn skull (by assigning it the optical properties of cartilage instead of bone) can have an impact on optical sensitivity. In order to distinguish the fontanel from the skull a CT scan (X-ray computed tomography) is necessary, as the two tissues are generally indistinguishable to standard MRI. Because of the use of ionizing radiation, CT is not usually performed clinically on infants. For this reason, there are few CT volumes available and we have not been able to account for the fontanels in our model.

In studies of the adult brain, a standardized coordinate system, such as the Talairach or MNI systems, can be used to analyze multi-subject data in a common coordinate space (Chau and McIntosh, 2005). Images of an individual are transformed to the common space to allow for inter-subject and inter-study comparisons. A standard newborn MRI atlas, like that built by Kuklisova-Murgasova et al. (2011), should ideally provide the equivalent standardized space for newborns. Unfortunately, there is still debate in the MRI community about which newborn MRI

atlas should define the reference space and how these coordinates will be transformed to be universally applied to different ages (Kazemi et al., 2007).

A simpler approach is, of course, to use the adult MNI space for infant studies. By transforming each infant brain to the adult MNI space, a location in the infant brain can be given in adult MNI coordinates, and the anatomy will broadly match. For example, a coordinate which identifies a location on the post-central gyrus in adults will also represent, approximately, a location on the post-central gyrus in infants. However, comparisons of the physiological importance of spatially equivalent brain regions between the infant and adult populations are clearly flawed (Wilke et al., 2003). To transform our models to match adult MNI coordinates would, of course, inflate the infant head models to the size of an adult brain, which is clearly not appropriate for diffuse optical approaches. Instead, our 4D infant head model is based on MRI data with the same axis definitions as the MNI coordinate system but without being transformed to match the adult anatomy. A coordinate in our meshes will therefore represent a very different physiological location than the same coordinate in an MNI-registered adult.

An additional application of our 4D optical head model is related to the important issue of optode positioning. Many applications of diffuse optical techniques target a very particular, and known, location in the brain. In such studies the goal is not to map a functional response, but to examine the response of a certain region to a particular stimulus. An example is the NIRS studies performed in an attempt to assess pain processing in infants (Slater et al., 2006). As it is common that the number of DOT channels is limited, determining where to place the sources and detectors on the scalp so as to best sample the region of interest is very important. This optical head model can be utilized to optimize probe location. By modeling photon migration for a variety of source and detector arrangements, the optical fiber array that best samples a given brain region can be determined. It is also possible to imagine an approach that takes advantage of the reciprocity of photon migration in tissue to explicitly calculate the best source and detector positions for sampling a given brain coordinate, rather than producing multiple models and choosing the most suitable.

Conclusion

We have presented a 4D optical head model package for preterm through to term newborns ranging from 29 to 44 weeks PMA, at one week intervals. This atlas is freely available online (www.ucl.ac.uk/medphys/research/4dneonatalmodel) and provides, for every age, 1) a multi-layered tissue mask including WM, GM, CSF, cerebellum, brainstem and extra-cerebral tissues, 2) a volumetric high-density tetrahedral head mesh, 3) GM, WM and scalp surface meshes and 4) cranial landmark coordinates and 10-5 locations. The package allows researchers to select, for every newborn under examination, an accurate age-matched head model, and thus aged-matched anatomy. This allows for maximally accurate optical image reconstruction and anatomically meaningful, uniform presentation of the resulting images. Ultimately this improves the quality, accuracy and interpretability of DOT images and will aid their application to neonatal medicine.

Acknowledgments

References

Abdelnour, F., Genovese, C., Huppert, T., 2010. Hierarchical Bayesian regularization of reconstructions for diffuse optical tomography using multiple priors. Biomed. Opt. Express 1 (4), 1084–1103.

Altaye, M., Holland, S.K., Wilke, M., Gaser, C., 2008. Infant brain probability templates for MRI segmentation and normalization. Neuroimage 43 (4), 721–730.

Ancora, G., Maranella, E., Grandi, S., Sbravati, F., Coccolini, E., Savini, S., Faldella, G., 2013. Early predictors of short term neurodevelopmental outcome in asphyxiated cooled infants. A combined brain amplitude integrated electroencephalography and near infrared spectroscopy study. Brain Dev. 35 (1), 26–31.

Arridge, S.R., 2011. Methods in diffuse optical imaging. Philos. Trans. A Math. Phys. Eng. Sci. 369 (1955), 4558–4576.

Austin, T., Hebden, J.C., Gibson, A.P., Branco, G., Yusof, R., Arridge, S.R., Meek, J.H., Delpy, D.T., Wyatt, J.S., 2006. Three dimensional optical imaging of blood volume and oxygenation in the neonatal brain. Neuroimage 31, 1426–1433.

Bade, R., Haase, H., Preim, B., 2006. Comparison of fundamental mesh smoothing algorithms for medical surface models. Proc. Simul. Vis. 289–304.

Barnett, A.H., Culver, J.P., Sorensen, A.G., Dale, A., Boas, D.A., 2003. Robust inference of baseline optical properties of the human head with three-dimensional segmentation from magnetic resonance imaging. Appl. Opt. 42 (16), 3095–3108.

Battin, M., Rutherford, M.A., 2002. Magnetic resonance imaging of the brain in preterm infants: 24 weeks' gestation to term. In: Rutherford, M.A. (Ed.), MRI of the Neonatal Brain. W.B. Saunders (chapter 3).

Boas, D.A., Dale, A.M., 2005. Simulation study of magnetic resonance imaging-guided cortically constrained diffuse optical tomography of human brain function. Appl. Opt. 44 (10), 1957–1968.

Boas, D.A., Franceschini, M.A., Dunn, A.K., Strangman, G., 2002. Noninvasive imaging of cerebral activation with diffuse optical tomography. In: Frostig, R.D. (Ed.), In Vivo Optical Imaging of Brain Function. CRC Press, pp. 193–221.

Boas, D.A., Dale, A.M., Franceschini, M.A., 2004. Diffuse optical imaging of brain activation: approaches to optimizing image sensitivity, resolution and accuracy. Neuroimage 23, S275–S288.

Chau, W., McIntosh, A.R., 2005. The Talairach coordinate of a point in the MNI space: how to interpret it. Neuroimage 25 (2), 408–416.

Collins, D.L., Zijdenbos, A.P., Kollokian, V., Sled, J.G., Kabani, N.J., Holmes, C.J., Evans, A.C., 1998. Design and construction of a realistic digital brain phantom. IEEE Trans. Med. Imaging 17 (3), 463–468.

Cooper, R.J., Hebden, J.C., O'Reilly, H., Mitra, S., Michell, A.W., Everdell, N.L., Gibson, A.P., Austin, T., 2011. Transient haemodynamic events in neurologically compromised infants: a simultaneous EEG and diffuse optical imaging study. Neuroimage 55 (4), 1610–1616.

Cooper, R.J., Caffini, M., Dubb, J., Fang, Q., Custo, A., Tsuzuki, D., Fischl, B., Wells 3rd, W., Dan, I., Boas, D.A., 2012. Validating atlas-guided DOT: a comparison of diffuse optical tomography informed by atlas and subject-specific anatomies. Neuroimage 62 (3), 1999–2006.

Costeloe, K.L., Hennessy, E.M., Haider, S., Stacey, F., Marlow, N., Draper, E.S., 2012. Short term outcomes after extreme preterm birth in England: comparison of two birth cohorts in 1995 and 2006 (the EPICure Studies). BMJ 345, e7976.

Culver, J.P., Siegel, A.M., Stott, J.J., Boas, D.A., 2003. Volumetric diffuse optical tomography of brain activity. Opt. Lett. 28 (21), 2061–2063.

Custo, A., Boas, D.A., Tsuzuki, D., Dan, I., Mesquita, R., Fischl, B., Grimson, W.E., Wells 3rd, W., 2010. Anatomical atlas-guided diffuse optical tomography of brain activation. Neuroimage 49 (1), 561–567.

Dehaes, M., Kazemi, K., Pélégrini-Issac, M., Grebe, R., Benali, H., Wallois, F., 2011. Quantitative effect of the neonatal fontanel on synthetic near infrared spectroscopy measurements. Hum. Brain Mapp. 34, 878–889.

Dehghani, H., Srinivasan, S., Pogue, B.W., Gibson, A., 2009. Numerical modeling and image reconstruction in diffuse optical tomography. Philos. Trans. R. Soc. 367, 3073–3093.

Eggebrecht, A.T., White, B.R., Ferradal, S.L., Chen, C., Zhan, Y., Snyder, A.Z., Dehghani, H., Culver, J.P., 2012. A quantitative spatial comparison of high-density diffuse optical tomography and fMRI cortical mapping. Neuroimage 61 (4), 1120–1128.

Elisee, J., Gibson, A.P., Arridge, S.R., 2011. Diffuse optical cortical mapping using the boundary element method. Biomed. Opt. Express 2, 568–578.

Elwell, C.E., Henty, J., Leung, T., Austin, T., Meek, J., Delpy, D., Wyatt, J., 2005. Regional measurements of CMRO2 in neonates undergoing intensive care using near infrared spectroscopy. Adv. Exp. Med. Biol. 566, 263–268.

Fang, Q., 2010. Mesh-based Monte Carlo method using fast ray-tracing in Plücker coordinates. Biomed. Opt. Express 1 (1), 165–175.

Fang, Q., Boas, D.A., 2009a. Tetrahedral mesh generation from volumetric binary and grayscale images. Proc. IEEE Int. Symp. Biomed. Imaging 2009, 1142–1145.

Fang, Q., Boas, D.A., 2009b. Monte Carlo simulation of photon migration in 3D turbid media accelerated by graphics processing units. Opt. Express 17 (22), 20178–20190.

Fang, Q., Kaeli, D.R., 2012. Accelerating mesh-based Monte Carlo method on modern CPU architectures. Biomed. Opt. Express 3 (12), 3223–3230.

Ferradal, S.L., Eggebrecht, A.T., Hassanpour, M., Snyder, A.Z., Culver, J.P., 2013. Atlas-based head modeling and spatial normalization for high-density diffuse optical tomography: in vivo validation against fMRI. Neuroimage S1053–8119 (13), 322–324.

Field, D.A., 2000. Qualitative measures for initial meshes. Int. J. Numer. Methods Eng. 47, 887–906.

Fonov, V.S., Evans, A.C., Botteron, K., Almli, C.R., McKinstry, R.C., Collins, D.L., BDCG, 2011. Unbiased average age-appropriate atlases for pediatric studies. Neuroimage 54 (1), 313–327.

Fournier, M., Mahmoudzadeh, M., Kazemi, K., Kongolo, G., Dehaene-Lambertz, G., Grebe, R., Wallois, F., 2012. Realistic head model design and 3D brain imaging of NIRS signals using audio stimuli on preterm neonates for intra-ventricular hemorrhage diagnosis. MICCAI 2012, Part III, LNCS 7512, pp. 172–179.

Fukui, Y., Ajichi, Y., Okada, E., 2003. Monte Carlo prediction of near-infrared light propagation in realistic adult and neonatal head models. Appl. Opt. 42 (16), 2881–2887.

Gibson, A.P., Hebden, J.C., Arridge, S.R., 2005. Recent advances in diffuse optical imaging. Phys. Med. Biol. 50 (4), R1–R43.

Gregg, N.M., White, B.R., Zeff, B.W., Berger, A.J., Culver, J.P., 2010. Brain specificity of diffuse optical imaging: improvements from superficial signal regression and tomography. Front. Neuroenerg. 2 (14).

Guven, M., Yazici, B., Intes, X., Chance, B., 2005. Diffuse optical tomography with a priori anatomical information. Phys. Med. Biol. 50 (12), 2837–2858.

Habermehl, C., Holtze, S., Steinbrink, J., Koch, S.P., Obrig, H., Mehnert, J., Schmitz, C.H., 2012. Somatosensory activation of two fingers can be discriminated with ultrahigh-density diffuse optical tomography. Neuroimage 59 (4), 3201–3211.

Heiskala, J., Pollari, M., Metsäranta, M., Grant, P.E., Nissilä, I., 2009. Probabilistic atlas can improve reconstruction from optical imaging of the neonatal brain. Opt. Express 17 (17), 14977–14992.

Heiskala, J., Kolehmainen, V., Tarvainen, T., Kaipio, J.P., Arridge, S.R., 2012. Approximation error method can reduce artifacts due to scalp blood flow in optical brain activation imaging. J. Biomed. Opt. 17 (9) (96012-1).

Hielscher, A.H., Bluestone, A.Y., Abdoulaev, G.S., Klose, A.D., Lasker, J., Stewart, M., Netz, U., Beuthan, J., 2002. Near-infrared diffuse optical tomography. Dis. Markers 18, 313–337.

Jenkinson, M., Pechaud, M., Smith, S., 2005. BET2: MR-based estimation of brain, skull and scalp surfaces. Eleventh Annual Meeting of the Organization for Human Brain Mapping, vol. 17.

Jöbsis, F.F., 1977. Noninvasive, infrared monitoring of cerebral and myocardial oxygen sufficiency and circulatory parameters. Science 198 (4323), 1264–1267.

Jurcak, V., Tsuzuki, D., Dan, I., 2007. 10/20, 10/10, and 10/5 systems revisited: their validity as relative head-surface-based positioning systems. Neuroimage 34 (4), 1600–1611.

Kazemi, K., Moghaddam, H.A., Grebe, R., Gondry-Jouet, C., Wallois, F., 2007. A neonatal atlas template for spatial normalization of whole-brain magnetic resonance images of newborns: preliminary results. Neuroimage 37 (2), 463–473.

Kuklisova-Murgasova, M., Aljabar, P., Srinivasan, L., Counsell, S.J., Doria, V., Serag, A., Gousias, I.S., Boardman, J.P., Rutherford, M.A., Edwards, A.D., Hajnal, J.V., Rueckert, D., 2011. A dynamic 4D probabilistic atlas of the developing brain. Neuroimage 54 (4), 2750–2763.

Ledig, C., Wolz, R., Aljabar, P., Lotjonen, J., Heckemann, R.A., Hammers, A., Rueckert, D., 2012. Multi-class brain segmentation using atlas propagation and EM-based refinement. Biomedical Imaging (ISBI), 2012 9th IEEE International Symposium on, pp. 896–899.

Liao, S.M., Ferradal, S.L., White, B.R., Gregg, N., Inder, T.E., Culver, J.P., 2012. High-density diffuse optical tomography of the term infant visual cortex in the nursery. J. Biomed. Opt. 17 (8), 081414.

Lin, P.Y., Roche-Labarbe, N., Dehaes, M., Carp, S., Fenoglio, A., Barbieri, B., Hagan, K., Grant, P.E., Franceschini, M.A., 2013. Non-invasive optical measurement of cerebral metabolism and hemodynamics in infants. J. Vis. Exp. 73, e4379.

Liu, A., Joe, B., 1994. Relationship between tetrahedron shape measures. BIT 34, 268–287.

Lloyd-Fox, S., Blasi, A., Elwell, C.E., 2010. Illuminating the developing brain: the past, present and future of functional near-infrared spectroscopy. Neurosci. Biobehav. Rev. 34 (3), 269–284.

Oishi, K., Mori, S., Donohue, P.K., Ernst, T., Anderson, L., Buchthal, S., Faria, A., Jiang, H., Li, X., Miller, M.I., van Zijl, P.C., Chang, L., 2011. Multi-contrast human neonatal brain atlas: application to normal neonate development analysis. Neuroimage 56 (1), 8–20.

Oostenveld, R., Praamstra, P., 2001. The five percent electrode system for high-resolution EEG and ERP measurements. Clin. Neurophysiol. 112 (4), 713–719.

Perdue, K.L., Fang, Q., Diamond, S.G., 2012. Quantitative assessment of diffuse optical tomography sensitivity to the cerebral cortex using a whole-head probe. Phys. Med. Biol. 57 (10), 2857–2872.

Pogue, B.W., Paulsen, K.D., 1998. High-resolution near-infrared tomographic imaging simulations of the rat cranium by use of a priori magnetic resonance imaging structural information. Opt. Lett. 23 (21), 1716–1718.

Prastawa, M., Gilmore, J.H., Lin, W., Gerig, G., 2005. Automatic segmentation of MR images of the developing newborn brain. Med. Image Anal. 9 (5), 457–466.

Sanchez, C.E., Richards, J.E., Almli, C.R., 2011. Neurodevelopmental MRI brain templates for children from 2 weeks to 4 years of age. Dev. Psychobiol. 54 (1), 77–91.

Schweiger, M., Arridge, S.R., 1999. Optical tomographic reconstruction in a complex head model using a priori region boundary information. Phys. Med. Biol. 44 (11), 2703–2721.

Schweiger, M., Arridge, S., 2014. The Toast++ software suite for forward and inverse modeling in optical tomography. J. Biomed. Opt. 19 (4), 040801.

Shi, F., Yap, P.T., Wu, G., Jia, H., Gilmore, J.H., Lin, W., Shen, D., 2011. Infant brain atlases from neonates to 1- and 2-year-olds. PLoS One 6 (4), e18746.

Singh, A.K., Okamoto, M., Dan, H., Jurcak, V., Dan, I., 2005. Spatial registration of multi-channel multi-subject fNIRS data to MNI space without MRI. Neuroimage 27 (4), 842–851.

Slater, R., Cantarella, A., Gallella, S., Worley, A., Boyd, S., Meek, J., Fitzgerald, M., 2006. Cortical pain responses in human infants. J. Neurosci. 26 (14), 3662–3666.

Tian, F., Liu, H., 2013. Depth-compensated diffuse optical tomography enhanced by general linear model analysis and an anatomical atlas of human head. Neuroimage S1053-8119 (13), 00771–00774.

Tsuzuki, D., Dan, I., 2013. Spatial registration for functional near-infrared spectroscopy: from channel position on the scalp to cortical location in individual and group analyses. Neuroimage S1053-8119 (13), 00780–00785.

Tsuzuki, D., Cai, D.S., Dan, H., Kyutoku, Y., Fujita, A., Watanabe, E., Dan, I., 2012. Stable and convenient spatial registration of stand-alone NIRS data through anchor-based probabilistic registration. Neurosci. Res. 72 (2), 163–171.

White, B.R., Culver, J.P., 2010. Quantitative evaluation of high-density diffuse optical tomography: in vivo resolution and mapping performance. J. Biomed. Opt. 15 (2), 026006.

White, B.R., Liao, S.M., Ferradal, S.L., Inder, T.E., Culver, J.P., 2012. Bedside optical imaging of occipital resting-state functional connectivity in neonates. Neuroimage 59 (3), 2529–2538.

Wilke, M., Schmithorst, V.J., Holland, S.K., 2003. Normative pediatric brain data for spatial normalization and segmentation differs from standard adult data. Magn. Reson. Med. 50 (4), 749–757.

Zhan, Y., Eggebrecht, A.T., Culver, J.P., Dehghani, H., 2012. Image quality analysis of high-density diffuse optical tomography incorporating a subject-specific head model. Front. Neuroenerg. 4 (6).

Zhang, X., Toronov, V., Webb, A., 2005. Simultaneous integrated diffuse optical tomography and functional magnetic resonance imaging of the human brain. Opt. Express 13 (14), 5513–5521.